Luminescent and Sublimable Binaphthyl-Based Field-Induced Lanthanide Single-Molecule Magnets

Carlo Andrea Mattei, Thomas Delouche, Bertrand Lefeuvre, Marie Cordier, Claudia Lalli, Olivier Cador, Laura Abad Galán, François Riobé, Olivier Maury, Pierre-Antoine Bouit, et al.

▶ To cite this version:

Carlo Andrea Mattei, Thomas Delouche, Bertrand Lefeuvre, Marie Cordier, Claudia Lalli, et al.. Luminescent and Sublimable Binaphthyl-Based Field-Induced Lanthanide Single-Molecule Magnets. Chemistry Squared, 2022, 6, pp.1. 10.28954/2022.csq.06.001 . hal-03798035

HAL Id: hal-03798035
https://hal.science/hal-03798035

Submitted on 5 Oct 2022

Luminescent and Sublimable Binaphthyl-Based Field-Induced Lanthanide Single-Molecule Magnets

Carlo Andrea Mattei [a], Thomas Delouche [a],
Bertrand Lefeuvre [a], Marie Dallon-Cordier [a], Claudia Lalli [a], Olivier Cador [a], Laura Abad Galán,
François Riobé [b],* Olivier Maury [b], Pierre-Antoine Bouit [a,*], Fabrice Pointillart [a,*]

Emails: francois.riobe@ens-lyon.fr, pierre-antoine.bouit@univ-rennes1.fr,
fabrice.pointillart@univ-rennes1.fr

[a] Univ Rennes, CNRS, ISCR (Institut des Sciences Chimiques de Rennes) – UMR 6226, 35000, Rennes (France)

[b] Univ Lyon, ENS de Lyon, CNRS UMR 5182, Laboratoire de Chimie, 69342, Lyon (France)

Abstract: The association of the [Ln(hfac)$_3$(H$_2$O)$_2$] metallic building blocks with the new ligand [1,1'-binaphthalene]-8,8'-diylbis(diphenylphosphine oxide) (**L**) led to the formation of three mononuclear complexes of formula [Ln(hfac)$_3$(**L**)] (Ln^{III} = Eu (**1**), Dy (**2**) and Yb (**3**)). The mononuclear character of the compounds is due to the bidentate coordination mode adopted by **L** to link the metal. **L** allows the observation of the characteristic visible $^5D_0 \rightarrow {}^7F_J$ (J = 0-4) Eu^{III}- and near infrared $^2F_{5/2} \rightarrow {}^2F_{7/2}$ Yb^{III}- emissions while **2** is only weakly emissive due to the mismatch between the energy positions of the triplet excited state of the ligand and Dy^{III} emissive state. The magnetic data reveal a field-induced Single-Molecule Magnet (SMM) behavior for **2** and **3** with an efficient suppression of the Quantum Tunneling of the Magnetization (QTM). The slow magnetic relaxation occurs through a Raman process while the Orbach contribution is discarded as confirmed by the correlation with the M$_J$ states energy splitting provided by the luminescence spectrum of **3**.

Keywords: Lanthanide, β-diketonate, Binaphthalene, Sublimation, Luminescence, Single-Molecule Magnet.

I. Introduction

Lanthanide ions are intensively used in coordination chemistry to design molecular materials able to display Single-Molecule Magnet (SMM) behavior [1] and luminescence [2]. Since these two physical properties have common electronic origin, magneto-luminescence correlations have been performed exploiting the experimental luminescence as a photography of the energy splitting of the ground $^{2S+1}L_J$ terms and allowing a rationalization of the magnetic properties [3-8]. On one side, the observation of a magnetic bistability up to 80 K [9] opens the way to potential applications in high density data storage [10] while on the other side the narrow emission bands and long lifetimes are studied for applications as thermal-sensors [11,12], electro-luminescence materials [13] and biomedical probes [14-15]. Restricting our scope to lanthanide SMMs, the addition of a third property such as the chirality could allow the observation of new physical properties. Indeed, Circularly Polarized Luminescence (CPL) [16-19], ferroelectricity [20], Magneto-Electric coupling (ME) [21] and Magneto-Chiral Dichroism (MCD) [22-23] have been already observed in lanthanide SMMs. The stereochemistry of the lanthanide ions is an issue because of the electrostatic character of the chemical interaction with the first surrounding, the high coordination number, low local symmetries and configurational lability. Thus, the chirality is often introduced via chiral ligands involving stereogenic elements to design chiral lanthanide SMMs. In such molecular objects, the chirality comes

doi: 10.28954/2022.csq.06.001

from a stereogenic center [24-25] helix [26] or axis [27]. In case of axial chirality, one of the most used ligands are the 2,2'-bis(diphenylphosphoryl)-1,1'-binaphthyl (BINAPO) and its bisphosphate analogues [28-32] because molecules bearing phosphine oxide groups are well known to efficiently coordinate Ln^{III} ions [33].

In this paper, it has appeared interesting to investigate the coordination chemistry of the molecule [1,1'-binaphthalene]-8,8'-diylbis(diphenylphosphine oxide) (8,8'-BINAPO, called later in the paper as **L**) (**Figure 1**) [34]. This ligand presents two oxygen basic sites which could be suitable for coordinating Lewis acids such as Ln^{III} centers. The relative position between the element of axial chirality and the phosphine oxide groups differs compared to the BINAPO and its bisphosphate analogues. This detail confers to **L** a peculiar structure, which is expected to affect its coordination chemistry and the properties of the final product. The structural, optical and magnetic properties of three compounds with formula [Ln(hfac)$_3$(**L**)] (Ln = Eu (**1**), Dy (**2**) and Yb (**3**)) are investigated in the following lines.

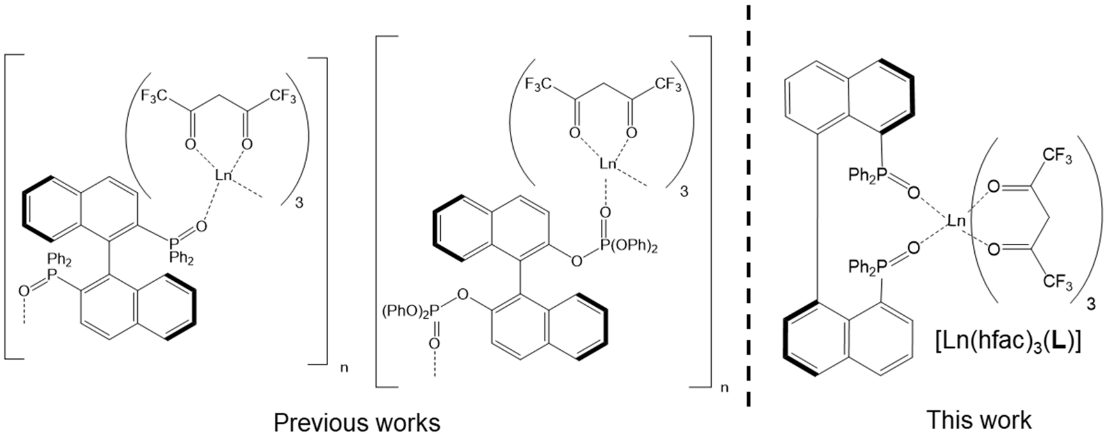

Figure 1. Examples of lanthanide coordination complexes involving BINAPO derived ligands (left) and structure of the compounds [Ln(hfac)$_3$(**L**)] with the ligand **L** studied in this article (right).

II. Results and Discussion

Synthesis. Ligand **L** was easily synthesized according to a straightforward synthesis involving a Cu-promoted C-C coupling of (8-bromonaphthalen-1-yl)diphenylphosphine oxide (yield: 77%) (**Scheme 1**). The ligand was fully characterized including X-ray diffraction (**Figure S1**). Enantiopure samples (with ee higher than 93%) of **L** were obtained via HPLC over a chiral stationary phase (see ESI). However, kinetic studies demonstrated that **L** racemizes in less than one hour at room temperature ($t_{1/2}$ = 38 min in DCM, **Figures S2-5**, **Table S1**). Thus, the coordination reactions with the $Ln(hfac)_3(H_2O)_2$ metal precursors (Ln^{III} = Eu, Dy and Yb) were carried out from a racemic mixture of ligand. This approach allows synthesizing a new family of lanthanide complexes featuring a novel BINAPO-like ligand. Attempts to separate the enantiomers of complexes Ln(hfac)$_3$(**L**) using HPLC failed leading to the collection of enantiomers of free ligands.

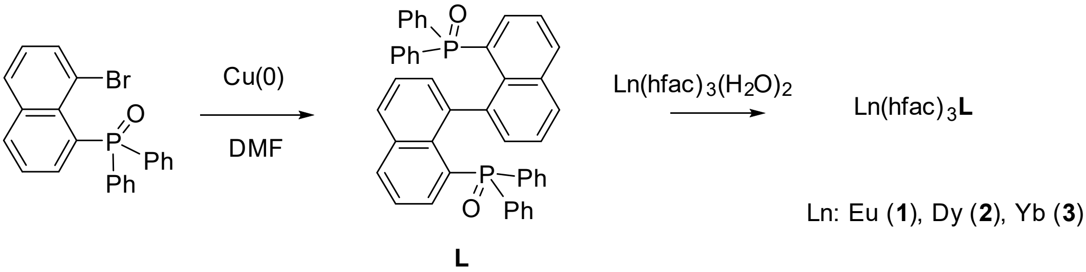

Scheme 1. Synthesis of ligand **L** and coordination complexes **1-3**.

Crystal Structure of complexes [Ln(hfac)$_3$(L)]. ORTEP view of **L** as well as the crystallographic data are given in the Supporting Information (**Figure S1** and **Table S2**). Crystalline products were collected in high yields by slow evaporation of the solvent from CH_2Cl_2/*n*-hexane solutions containing equimolar quantities of the reagents. The quality of the Dy^{III}-based crystals allowed their structural characterization by Single Crystal X-Ray Diffraction analysis (SCXRD, **Table S2**). The ligand **L** acts as a bis-chelate agent substituting the two water molecules and forming mononuclear complexes (**Figure 2**). Such coordination mode contrasts with what was observed with BINAPO [29] and BINOL-derived bisphosphate [31,32] ligands for which the bis-monodentate coordination mode led to the formation of mono-dimensional polymers. Therefore, the Dy^{III} ion is octa-coordinated by six oxygen atoms from three ligands hfac$^-$ and two oxygen atoms from the two phosphine oxide groups of one ligand **L**. The asymmetric unit contains a total of three mononuclear complexes according with the chemical formula [Dy(hfac)$_3$(**L**)] (**Figure S6**). Dy-O$_{hfac}$ distances display an average value of 2.367(5) Å which is slightly longer than the average Dy-O$_{P=O}$ length of 2.278(7) Å. The dihedral angles between the naphthyl groups have close values equal to 156.5(2)°, 157.3(4)° and 158.4(4)° when the ligand is coordinated to the centers Dy1, Dy2 and Dy3 centers, respectively. SHAPE analysis [35] indicates that the coordination polyhedra of the three crystallographic centers can be described by slightly distorted (compressed) D_{4d} symmetries with similar deviation from ideal polyhedron (**Table S3**). The unit cell is composed by six pairs of enantiomers for twelve molecules in total (**Figure S7**). Indeed, the final product is a racemic mixture and it crystallizes in the monoclinic space group $P2_1/c$ (N° 14). The shortest Dy···Dy distance is equal to 10.49(9) Å. The molecular units are disposed in the crystal packing alternating their orientation as a consequence of an intricate network of π···CH, CH···CH, F···H and F···F interactions. Powder X-Ray diffraction (PXRD) studies are in good agreement with the calculated diffractogram indicating the presence of only one crystalline phase (**Figure S8a**). Compounds **1** and **3** are isostructural to **2** as demonstrated by PXRD studies (**Figure S8a**).

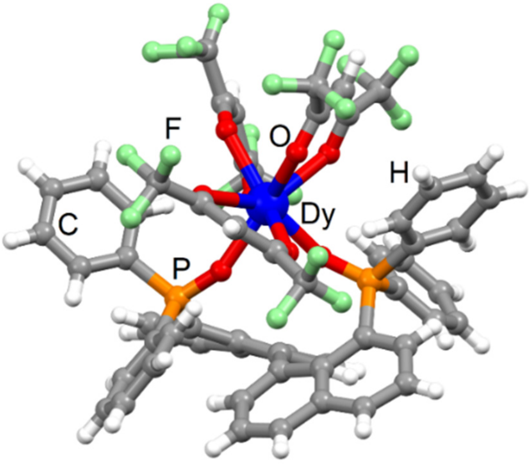

Figure 2. Single Crystal X-ray Diffraction structure of the mononuclear complex [Dy(hfac)$_3$(**L**)]. Color codes: H, white; C, gray; F, green; O, red; P, orange; Dy, blue.

All these compounds resulted highly soluble in classical organic solvents such as 1,2-dichloroethane and toluene. The monomeric species [Ln(hfac)$_3$(**L**)], thanks to their high degree of fluorination, were expected to be enough volatile for sublimating in the appropriate conditions. Indeed, grained crystals of the complexes [Ln(hfac)$_3$(**L**)] sublimated quantitatively when heated at 270–280 °C at reduced pressure (10 mbar). The volatile phases were collected on a cold finger and characterized by IR spectroscopy and PXRD analysis displaying a good agreement with the spectra and diffractograms of the starting compounds (**Figure S8b**). The PXRD diffractograms also highlight the crystallinity of the sublimated species. Moreover, their similar shapes (relative intensities) suggest a certain homogeneity of the microcrystals size. Nevertheless such a technique did not allow the obtention of big enough single crystals for SCXRD studies.

Optical Studies. The excitation spectra and metal-centered emission for **1** are reported in **Figure S9**. The room (gray line) and low (orange) temperature measurements do not display any significant change of the broad ligand bands. The characteristic $^5D_0 \rightarrow {}^7F_J$ with $J = 0, 1, 2, 3$ and 4 emission bands for the Eu^{III} ion are observed and their most intense signals fall around 17271 cm^{-1} (579 nm), 16835 cm^{-1} (594 nm), 16313 cm^{-1} (613 nm), 15243 cm^{-1} (656 nm) and 14925 cm^{-1} (670 nm), respectively. Recording the spectrum at 77 K allows for a slightly better resolution compared to the room temperature measurement. The $^5D_0 \rightarrow {}^7F_0$ transition can be observed and the $^5D_0 \rightarrow {}^7F_1$ and $^5D_0 \rightarrow {}^7F_2$ transitions are split in three and at least four signals, respectively, which are higher numbers than observed for perfect D_{4d} symmetries [36]. The ratio R of the intensities of the $^5D_0 \rightarrow {}^7F_1$ and $^5D_0 \rightarrow {}^7F_2$ transitions ($R = I(^5D_0 \rightarrow {}^7F_2)/I(^5D_0 \rightarrow {}^7F_1)$) is found equal to 24.6 units. This value is close to those found for Eu^{III} compounds involving chiral 1,1'-bi-2-naphthol-derived bisphosphate ligands [36]; moreover a value of $R > 10$ is often observed for Eu^{III} β-diketonate complexes [37]. The emission lifetime curves can be fit with a mono-exponential decay function affording lifetime constants around 700 µs at both room temperature and 77 K (**Figure S10**). The excitation spectrum at room temperature for **2** is similar to that for **1** (**Figure S7**). Excitation of **2** at 26667 cm^{-1} (375 nm) or 30769 cm^{-1} (325 nm) led to the observation of a broad band centered at 25126 cm^{-1} (398 nm) (**Figure S11**). The lack of Dy^{III} luminescence may be due to an inefficient sensitization process caused by the too low energy position of the triplet excited state of the ligand **L** [32].

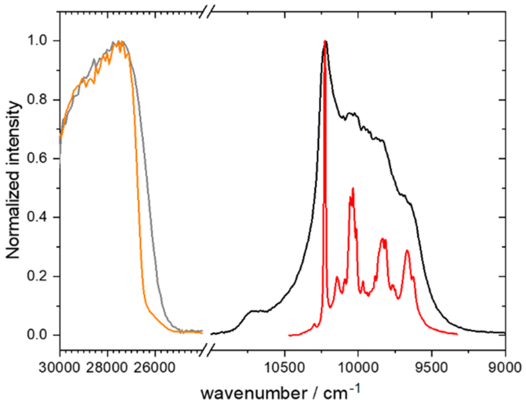

Figure 3. Solid state excitation spectrum recorded at room temperature (gray line) and 77 K (orange line) and solid state emission spectra recorded at room temperature (black line) and 77 K (red line) for **3**.

The excitation spectra for the complex **3** at both room and low temperatures were recorded in correspondence of the strongest Yb^{III} emission signal (**Figure 3**). The emission properties were studied by exciting the samples at 26667 cm^{-1} (375 nm), where it is located the tail of the hfac$^-$ absorption band [38]. Solid state measurements for **3** show the characteristic $^2F_{5/2} \rightarrow {}^2F_{7/2}$ transition expected for a Yb^{III} ion (**Figure 3**).

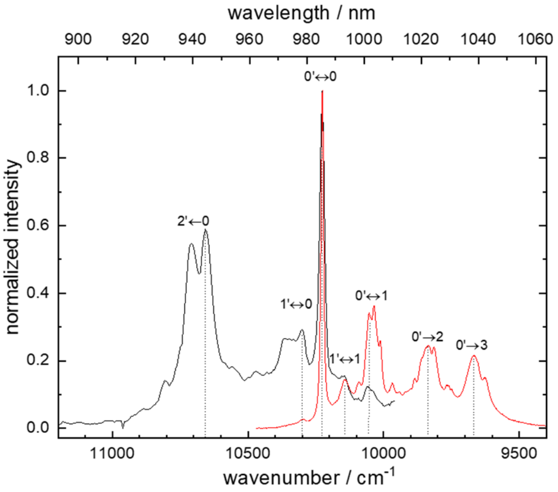

Figure 4. Overlay of the excitation and emission spectra at 77 K of **3**, corresponding to the $^2F_{5/2} \leftrightarrow {}^2F_{7/2}$ transition. The dotted lines indicate the proposed position of each transition.

Upon cooling down the sample at 77 K the luminescence spectrum appears extremely resolved and composed of four main signals centered at 10225 cm^{-1} (978 nm), 10035 cm^{-1} (995 nm), 9836 cm^{-1} (1017 nm) and 9671 cm^{-1} (1034 nm). These signals are representative of the $^2F_{7/2}$ multiplet splitting. The total splitting is 552 cm^{-1} is in agreement with the distorted D_{4d} symmetry observed for the Dy^{III} analogue X-Ray structure [39,40]. Additional contributions could be assigned to emissions from both the thermally populated excited M_J state of the $^2F_{5/2}$ multiplet and vibronic transitions (not present for the 0-0' transition at 10225 cm^{-1}). Thanks to a high-resolution excitation spectrum of the $^2F_{5/2} \leftarrow {}^2F_{7/2}$ transition (**Figure 4**), a complete energy diagram can be proposed (**Figure 5a**). It confirms that hot bands should be observed at 77 K according to the determination of the Boltzmann distribution in excited $^2F_{5/2}$ (**Figure 5b** and **Table S4**) where 19% of thermally populated 1' is present at 77 K. Emission spectra at 77 K of frozen solution of **3** in either dichloromethane or poly(methyl methacrylate) (PPMA) matrix (**Figure S12**) show the same overall shape than for the crystalline solid. It confirms that the additional bands are not due the three slightly different conformations observed at the solid state but probably to vibronic coupling at the molecular scale.

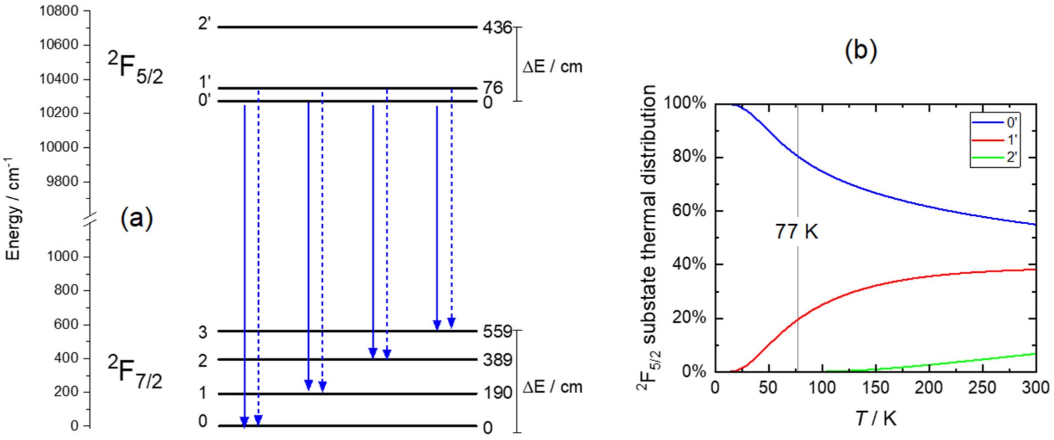

Figure 5. (a) Proposed energy diagram of **3** from the observation of the $^2F_{5/2} \leftrightarrow {}^2F_{7/2}$ transition; (b) corresponding evolution of the distribution of excited states in $^2F_{5/2}$ as a function of the temperature (detailed in **Table S3**).

Magnetic Studies. **Static Magnetic Measurements**. The $\chi_M T$ temperature dependences for the complexes **2** and **3** are reported in **Figure S13**. The room temperature values are 13.86 cm^3 K mol^{-1} and 2.37 cm^3 K mol^{-1} for the Dy^{III} and Yb^{III} -based species, respectively. These experimental data are slightly lower than the theoretically expected values of 14.17 cm^3 K mol^{-1} and 2.57 cm^3 K mol^{-1} for one isolated Dy^{III} ($^6H_{15/2}$ ground state multiplet) and Yb^{III} ($^2F_{7/2}$ ground state multiplet), respectively [41]. Upon cooling down at 2 K, the $\chi_M T$ values decrease monotonically to 11.56 cm^3 K mol^{-1} for **2** and 1.21 cm^3 K mol^{-1} for **3** (**Figure S13**). Such deviations from the Curie law can be explained by the thermal depopulation of the M_J states. Indeed, the presence of antiferromagnetic interactions can be reasonably excluded due to the considerable distances between the Ln^{III} ions in the crystal structure. The field dependences of the magnetization are measured at 2 K and represented in **Figure S14**. The values reached under a magnetic field of 50 kOe are 5.26 Nβ and 1.58 Nβ for **2** and **3**. For both compounds, these values are far from the expected theoretical saturation values of 10 Nβ and 4 Nβ for isolated Dy^{III} and Yb^{III} ions, respectively, in the absence of magnetic anisotropy.

Dynamic Magnetic Measurements. Dynamic studies of the magnetization were conducted on both **2** and **3** samples to confirm their SMM nature. No clear maxima for the out-of-phase (χ_M") signals were observed in zero magnetic field. However, the application of a static magnetic field at 2 K allowed the slow relaxation of the magnetization (**Figure 6a** and **6b**). Indeed, the values of the in-phase (χ_M') (**Figures S15-S16**) and out-of-phase signals decrease and increase, respectively, with increasing the frequency (ν). In the case of the compound **2**, a second contribution to the slow relaxation of the magnetization appears at low frequencies when a magnetic field between 1400 Oe and 3000 Oe is applied while for **3**, two contributions are observed under a modest field of 200 Oe and disappear for higher fields.

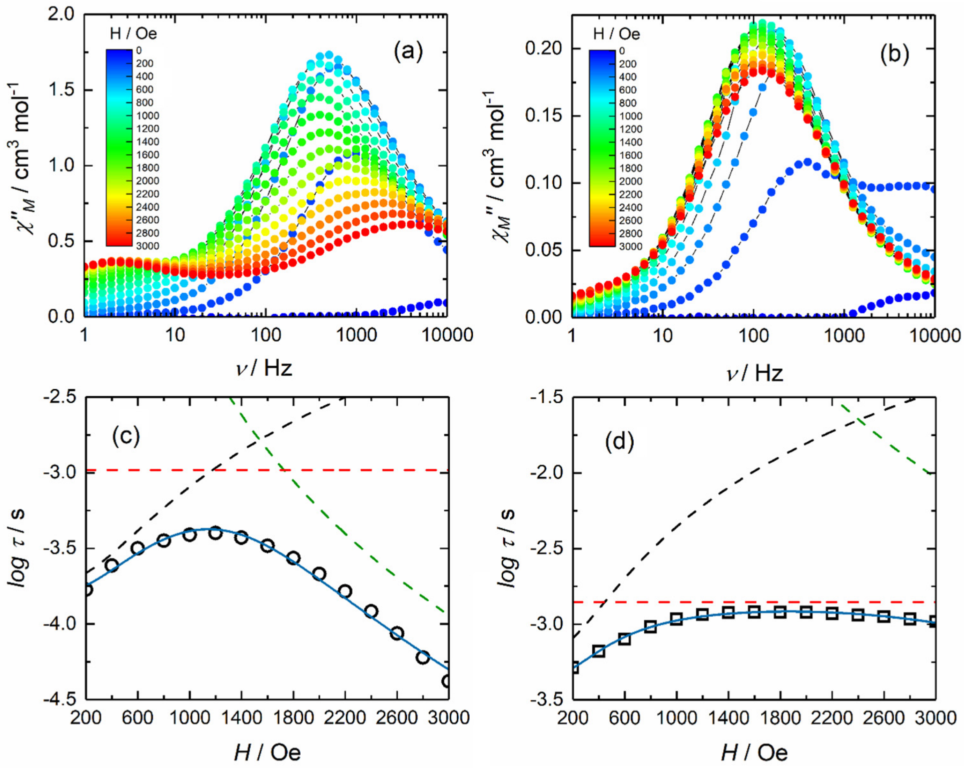

Figure 6. Frequency dependence of χ_M" between 0 and 3000 Oe at 2 K for **2** (a) and **3** (b). Field dependence of the relaxation times for **2** (open circles) (only high frequency contribution) (c) and **3** (open squares) (for 200 Oe, only the high contribution is considered) (d) between 200 and 3000 Oe at 2 K. The blue line is the best fitted curve. Each relaxation process is represented as follows: QTM (black dashed line), Direct (green dashed line) and thermally activated k(T) contribution (red dashed line). Parameters given in the text.

This behavior is often attributed to the presence of magnetic dipolar interactions between the lanthanide ions [42] but remain unusual for Yb^{III} magnetic centers. To better discuss the field dependence of the magnetic susceptibility, the experimental curves were analyzed in the context of extended Debye models (**Figure S17, Table S5-S6**). The extracted magnetic relaxation times τ at high frequency are reported in **Figure 6c-6d**. For **2**, the magnetization relaxation rate initially decreases with increasing the field until reaching a minimum value and slowly starting to increase again. This behavior suggests the presence of two different relaxation mechanisms, one minimized and the other maximized by the applied static field. Such observations are coherent with relaxation via QTM at low static magnetic fields followed by the activation of a Direct mechanism for stronger fields. The high frequency contribution of **3** displays a similar field dependence of the relaxation but with a less pronounced increase of the relaxation rate at high fields. Before reaching the maxima of the log τ vs H plots, both compounds relax with comparable rates. Equation 1 allows a fit procedure of the data.

$$\tau^{-1}(T,H) = AH^4T + \frac{B_1}{1+B_2H^2} + \underbrace{\tau_0^{-1}\,e^{\left(\frac{U_{eff}}{k_BT}\right)} + CT^n}_{k(T)} \qquad \text{Equation 1}$$

From left to right, the terms are the expressions of Direct, QTM and thermally activated (Orbach + Raman) contributions. The best fit parameters for **2** are $B_1 = 5.2(6) \times 10^3\ s^{-1}$, $B_2 = 3(1) \times 10^{-6}\ Oe^{-2}$, $A = 5.4(3) \times 10^{-11}\ s^{-1}\ K^{-1}\ Oe^{-4}$ and $k(T) = 1.0(4) \times 10^3\ s^{-1}$ (**Figure 6c**). The best fit parameters for **3** are $B_1 = 1.51(6) \times 10^3\ s^{-1}$, $B_2 = 5.7(6) \times 10^{-6}\ Oe^{-2}$, $A = 6.6(6) \times 10^{-13}\ s^{-1}\ K^{-1}\ Oe^{-4}$ and $k(T) = 7.2(1) \times 10^2\ s^{-1}$ (**Figure 6d**).

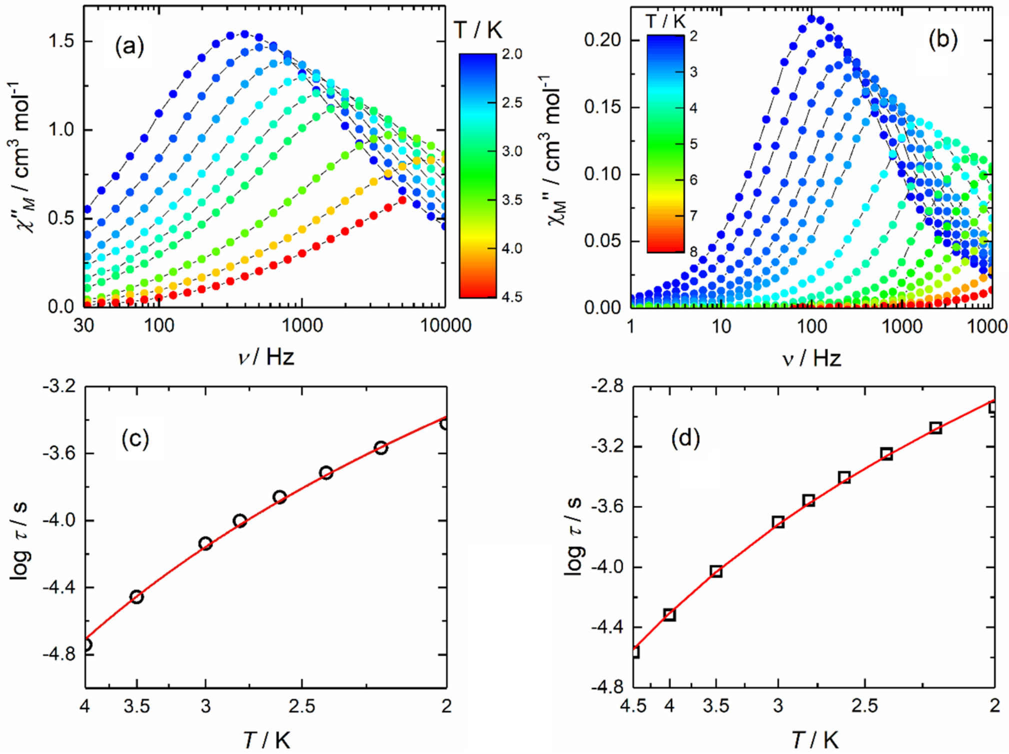

Figure 7. Frequency dependence of χ_M" at 800 Oe in the temperature range 2-4.5 K for **2** (a) and at 1200 Oe in the temperature range 2–8 K for **3** (b). Temperature variations of the relaxation times for **2** in the range 2–4 K under 800 Oe (open circles), and for **3** in the range of 2–4.5 K under 1200 Oe (open squares). The red lines depict the best fits by considering a Raman relaxation process. Parameters are given in the text.

The values of 800 Oe and 1200 Oe were selected to study the temperature dependent behavior of the magnetization for **2** and **3** compounds, respectively. Under these magnetic fields the QTM processes should be efficiently reduced and no Direct mechanism should be active. For both samples, the maxima of the out-of-phase signals move to higher frequencies with increasing the temperature (**Figures S18**, **S19** and **Figure 7**). A fitting procedure was performed by applying a simple extended Debye model (**Figures S20**, **S21**, **Tables S7**, **S8**). The obtained α values are in the range 0.25–0.31 for **2** and 0.02–0.20 for **3**. The larger α values for **2** could be ascribed to the richer isotopic composition of natural abundant dysprosium compared to ytterbium. The normalized Argand plots show that the out-of-phase components of the magnetic susceptibility represent the totality of the relaxing magnetic systems (**Figures S22**, **S23**). Therefore, it can be deduced that the three different crystallographic centers display a similar magnetic behavior. This is not surprising considering that i) all the coordination polyhedra calculated by SHAPE analysis can be described by similar a degree of distortion from the same ideal polyhedron and ii) the energy splitting for the Yb^{III} ions are similar as demonstrated with the emission investigation. The magnetic relaxation times were extracted and are represented in **Figure 7c**, **7d** as log(τ) vs T. The high temperature data could be fitted by the Eq. 1 by considering an Orbach process. The fitted parameters are τ_0 = 3.6(7) × 10^{-7} s and U_{eff} = 11.0(5) cm^{-1} (16 K) for **2** and τ_0 = 3.6(5) × 10^{-7} s and U_{eff} = 13.5(5) cm^{-1} (20 K) for **3**. However, the thermal energy of the systems (≤ 5 K in the experimental temperature ranges) reasonably excludes the participation of such Orbach contributions to the magnetization relaxation for both compounds. Moreover, the energy difference between the lowest M_J states determined from the experimental luminescence spectrum of **3** is equal to 190 cm^{-1}, a value much larger than the effective barrier. This confirms the exclusion of an Orbach process in the magnetization relaxation dynamic for **3**. A further possibility is to consider an active Raman process. The best fits are obtained with C = 110(10) and n = 4.4(1) for **2** and C = 30(2) and n = 4.70(7) for **3** (**Figure 7**). This would suggest that tunneling phenomena were efficiently suppressed by the selected static magnetic fields. The values of the Raman exponents are similar but lower than the theoretical expected ones [43]. A participation of optical phonons in the relaxation process is generally proposed to justify such deviations [44]. The Yb^{III} and Dy^{III} ions display approximately prolate and oblate electronic spatial distributions, respectively. Therefore, the same crystal field should generate a different SMM behavior. Despite this, both compounds exhibit slow relaxation of the magnetization with comparable rates (the Yb^{III} derivative relaxes about 1.2 times slower than the Dy^{III} one at 2 K and under the selected fields). The answer to this apparent anomaly may be researched in the magnetic relaxation mechanism, which is mainly Raman in the examined cases under optimal field conditions**.** Indeed, the magnetization relaxation is mediated by a phonon exchange occurring via virtual states. The energy location of such virtual states should be strongly dependent on the nature (chemical and structural composition) of the matrix [45] and the molecular vibration system [46,47] which are similar for the two species.

III. Conclusions

Three monomeric complexes with formula [Ln(hfac)$_3$(**L**)] were synthetized with the metals Eu (**1**), Dy (**2**) and Yb (**3**) coordinated to a new ligand **L** derived from the binaphthyl skeleton. SCXRD studies demonstrated the ability of the ligand **L** to chelate the metal centers through the donor oxygen atoms of the phosphine oxide groups. Each metal coordination sphere was completed by three $hfac^-$ ligands, which are known to increase the volatility in lanthanide compounds. Indeed, the prepared coordination compounds were sublimated as confirmed by PXRD analyses. Compounds **2** and **3** displayed a similar field-induced SMM behavior mainly relaxing through a Raman mechanism. The external magnetic fields applied for studying the τ thermal dependence efficiently reduced the participation of QTM processes without activating Direct relaxation pathways. Compound **1** exhibited solid state metal-centered emission at both, room temperature and 77 K. The NIR-emission $^2F_{5/2} \rightarrow {}^2F_{7/2}$ transition for the Yb^{III}-based compound was analyzed at 77 K in solid state. This allowed a direct visualization of the magnetic ground state. An analysis of the splitting value between the lowest M_J states corroborated the exclusion of any Orbach processes in the magnetization relaxation for **3**. Therefore, **3** exhibited both SMM behavior and luminescence in the solid state. Attempts to prepare enantiopure complexes of lanthanide with **L** to take advantage of their chiroptical properties are in progress in our laboratory using complexation at low temperature or in solvent free conditions.

IV. Additional Information

Supporting information is available online. Correspondence and requests for materials should be addressed to the corresponding author. Crystallographic data, crystal structure, PXRD data, SHAPE analyses, emission data for **1** and **2**, magnetic measurements and fitting data. CCDC 2116505 (**L**) and CCDC 2116506 (**2**) contains supplementary crystallographic data for this article. These data can be obtained free of charge from the Cambridge Crystallographic Data Centre via www.ccdc.cam.ac.uk/data_request/cif.

V. Materials and Methods

General Procedures and Materials. The precursor [Ln(hfac)$_3$(H$_2$O)$_2$] (hfac$^-$ = 1,1,1,5,5,5-hexafluoroacetylacetonate anion) [48] and (8-bromonaphthalen-1-yl)diphenylphosphine oxide [49] were synthesized following previously reported methods. All other reagents were commercially available and used without further purification.

Synthesis of L. (8-bromonaphthalen-1-yl)diphenylphosphine oxide (100 mg, 0.25 mmol, 1 eq) and Cu(0) (31 mg, 0.5 mmol, 2 eq) are dissolved in 10 mL mL of DMF. Then the reaction is heated to 160 °C overnight. Then, DMF is evaporated and the crude mixture was purified by silica gel chromatography using DCM/AcOEt (1/1) to afford **L** as a white powder. ^{1}H NMR (300 MHz, CD$_2$Cl$_2$) (**Figure S24**): δ 7.95 (d, *J* = 8.0 Hz, 2H), 7.64 (d, *J* = 8.2 Hz, 2H), 7.6 –7.12 (m, 24H), 6.73 (dd, *J* = 7.1, 1.6 Hz, 2H), 6.59 (t, *J* = 7.6 Hz, 2H). ^{13}C NMR (75 MHz, CD$_2$Cl$_2$) (**Figure S25**): δ 141.5, 138.7 (d, *J* = 107.6 Hz), 137.8 (d, *J* = 13.9 Hz), 136.6 (d, *J* = 6.2 Hz), 135.6 (d, *J* = 9.0 Hz), 135.4 (d, *J* = 102.6 Hz), 133.9, 131.7 (d, *J* = 9 Hz), 131.3 (d, *J* = 6 Hz) 129.4, 128.3 (d, *J* = 11.8 Hz), 128.0 (d, *J* = 11.9 Hz), 124.7, 122.9 (d, *J* = 15.3 Hz). ^{31}P NMR (121 MHz, Methylene Chloride-*d*$_2$) (**Figure S26**) δ + 33.7. HRMS (ESI, CH$_3$OH/CH$_2$Cl$_2$) [M+H]$^+$ (C$_{44}$H$_{33}$O$_2$P$_2$) : m/z Theoretical : 655.1950, m/z Found : 655.1948.

Synthesis of complex [Ln(hfac)$_3$(L)]. [Eu(hfac)$_3$(L)] (1). A solution containing 32.4 mg (0.04 mmol) of [Eu(hfac)$_3$(H$_2$O)$_2$] in 5 mL of CH$_2$Cl$_2$ was added to a solution containing 26.2 mg (0.04 mmol) of **L** in 5 mL of CH$_2$Cl$_2$. After 15 minutes of stirring, 30 mL of n-hexane were layered. After several days, the solution was slowly evaporated leading to colorless crystals. 44.0 mg, 77 % yield for **1**. IR (KBr, range 3200–400 cm^{-1}): 3061 (w), 1658 (s), 1596 (w), 1552 (m), 1526 (m), 1514 (m), 1499 (m), 1438 (m), 1359 (w), 1315 (w), 1257 (s), 1200 (s), 1171 (s), 1144 (s), 1115 (m), 1102 (m), 1071 (w), 1053 (w), 1029 (w), 999 (w), 982 (w), 950 (w), 929 (w), 828 (m), 794 (m), 776 (m), 750 (m), 723 (m), 692 (m), 662 (m), 587 (m), 544 (m), 528 (m), 513 (w), 501 (w), 467 (w), 424 (w) cm^{-1}. Anal. Calcd (%) for C$_{59}$H$_{35}$EuF$_{18}$O$_8$P$_2$: C 49.59, H 2.45; found: C 49.51, H 2.51. Grained crystals of the product sublimated quantitatively when heated around 270-280 °C at reduced pressure. IR spectrum and PXRD diffractogram of the sublimate were in good agreement with the spectrum and diffractogram of the starting material.

[Dy(hfac)$_3$(L)] (2). A solution containing 32.8 mg (0.04 mmol) of [Dy(hfac)$_3$(H$_2$O)$_2$] in 5 mL of CH$_2$Cl$_2$ was added to a solution containing 26.2 mg (0.04 mmol) of **L** in 5 mL of CH$_2$Cl$_2$. After 15 minutes of stirring, 30 mL of *n*-hexane were layered. After several days, the solution was slowly evaporated leading to colorless crystals. 47.7 mg, 83 % yield for **2**. I.R. (KBr; range 3200–400 cm^{-1}): 3062 (w), 1658 (s), 1596 (w), 1552 (m), 1526 (m), 1511 (m), 1499 (m), 1438 (m), 1359 (w), 1315 (w), 1257 (s), 1197 (s), 1171 (s), 1144 (s), 1115 (m), 1102 (m), 1071 (w), 1053 (w), 1029 (w), 999 (w), 982 (w), 950 (w), 929 (w), 828 (m), 794 (m), 776 (m), 750 (m), 723 (m), 692 (m), 660 (m), 584 (m), 544 (m), 528 (m), 513 (w), 501 (w), 467 (w), 424 (w) cm^{-1}. Anal. Calcd (%) for C$_{59}$H$_{35}$DyF$_{18}$O$_8$P$_2$: C 49.22, H 2.43; found: C 49.39, H 2.40. Grained crystals of the product sublimated quantitatively when heated around 270–280 °C at reduced pressure. IR spectrum and PXRD diffractogram of the sublimate were in good agreement with the spectrum and diffractogram of the starting material.

[Yb(hfac)$_3$(L)] (3). A solution containing 32.8 mg (0.04 mmol) of [Yb(hfac)$_3$(H$_2$O)$_2$] in 5 mL of CH$_2$Cl$_2$ was added to a solution containing 26.2 mg (0.04 mmol) of **L** in 5 mL of CH$_2$Cl$_2$. After 15 minutes of stirring, 30 mL of n-hexane were layered. After several days, the solution was slowly evaporated leading to colorless crystals. 40.8 mg, 70 % yield for **3**. I.R. (KBr, range 3200–400 cm^{-1}): 3063 (w), 1655 (s), 1596 (w), 1552 (m), 1525 (m), 1509 (m), 1499 (m), 1438 (m), 1359 (w), 1315 (w), 1257 (s), 1200 (s), 1166 (s), 1144 (s), 1114 (m), 1100 (m), 1071 (w), 1053 (w), 1029 (w), 999 (w), 982 (w), 950 (w), 929 (w), 826 (m), 794 (m), 776 (m), 750 (m), 723 (m), 692 (m), 660 (m), 584 (m), 544 (m), 528 (m), 513 (w), 501 (w), 464 (w), 424 (w) cm^{-1}. Anal. Calcd (%) for $C_{59}H_{35}YbF_{18}O_8P_2$: C 48.87, H 2.42; found: C 48.97, H 2.38. Grained crystals of the product sublimated quantitatively when heated around 270-280 °C at reduced pressure. IR spectrum and PXRD diffractogram of the sublimate were in good agreement with the spectrum and diffractogram of the starting material.

Crystallography. Single crystals of **L** and **2** were mounted on a D8 VENTURE Bruker-AXS diffractometer for data collection (MoK$_\alpha$ radiation source, $\lambda = 0.71073$ Å), from the Diffractometric center X (CDIFX), University of Rennes 1, France (Table S1). SHELXT program [50] was used to solve the structures with a direct method and refinements were done with the SHELXL-14/7 program [51] using a full matrix least-squares method on F^2. X-ray diffraction (XRD) patterns were recorded at room temperature in the 2θ range 5–30° with a step size of 0.026° and a scan time per step of 600 s using a PANalytical X'Pert Pro diffractometer (Cu-L2, L3 radiation, $\lambda = 1.5418$ Å, 40 kV,40 mA, PIXcel 1D detector). Data collector and HighScore Plus softwares were used, respectively, for recording and analysis of the patterns.

Physical Measurements. The elemental analyses of the compounds were performed at the Centre Régional de Mesures Physiques de l'Ouest, Rennes. ^{1}H NMR, ^{13}C NMR and ^{31}P NMR spectra were recorded using Bruker Avance spectrometers at 400 MHz for ^{1}H NMR, 75 MHz for ^{13}C NMR and 162 MHz for ^{31}P NMR. Chemical shifts (δ) are reported in parts per million (ppm) relative to TMS. The coupling constants (J) are given in hertz (Hz) and the corresponding multiplicity (s = singlet, d = doublet, t = triplet, m = multiplet). The static susceptibility measurements were performed on solid polycrystalline samples with a Quantum Design MPMS-XL SQUID magnetometer. The following values of magnetic field were used: 0.2 kOe, 2 kOe and 10 kOe, respectively, for the temperature range of 2–20 K, 20–80 K and 80–300 K, in order to prevent any saturation effect in case of **2,** while 2 kOe and 10 kOe are used for the temperature range of 2–20 K and 20–300 K for **3**. The ac magnetic susceptibility measurements were performed on both Quantum Design MPMS-XL SQUID magnetometer (1–1000 Hz frequency range) and Quantum Design PPMS 14 T magnetometer (100–10000 Hz frequency range). Immobilized selected and crunched single crystals were employed to perform the magnetic measurements and the latter were all corrected for the diamagnetic contribution as calculated with Pascal's constants.

VI. Conflict of Interests

The authors declare no competing financial interests.

VII. Acknowledgements

This work was supported by CNRS, Université de Rennes 1, and the European Commission through the ERC-CoG 725184 MULTIPROSMM (project n. 725184). T. Roisnel is thanked for the X-ray structure of **L**. N. Vanthuyne is thanked for the kinetic study on **L**.

VIII. References

[1] Woodruff, D. N.; Winpenny, R. E. P.; Layfield, R. A., *Chem. Rev.*, **2013**, *113*, 5110–5148.

[2] de Bettencourt-Dias, A. *Luminescence of lanthanide ions in coordination compounds and nanomaterials*, John Wiley & Sons, Ltd, **2014**.

[3] Pointillart, F.; Le Guennic, B.; Cador, O.; Maury, O.; Ouahab, L., *Acc. Chem. Res.*, **2015**, *48*, 2834–2842.

[4] Long, J.; Guari, Y.; Ferreira, R. A. S.; Carlos, L. D.; Larionova, J., *Coord. Chem. Rev.*, **2018**, *363*, 57–70.

[5] Jia, J.-H.; Li, Q.-W.; Chen, Y.-C.; Liu, J.-L.; Tong, M.-L., *Coord. Chem. Rev.*, **2019**, *378*, 365–381.

[6] Marin, R.; Brunet, G.; Murugesu, M., *Angew. Chem., Int. Ed.*, **2021**, *60*, 1728-1746.

[7] Errulat, D.; Marin, R.; Galico, A. M.; Harriman, K. L. M.; Pialat, A.; Gabidullin, B.; Iikawa, F.; Couto Jr., O. D. D.; Moilanen, J. O.; Hemmer, E.; Sigoli, F. A.; Murugesu, M., *ACS Cent. Sci.,* **2019**, *5*, 1187.

[8] Wang, J.; Zakrzewski, J. J.; Heczko, M.; Zychowicz, M.; Nakagawa, K.; Nakabayashi, K.; Sieklucka, B.; Chorazy, S.; Ohkoshi, S., *J. Am. Chem. Soc.*, **2020**, *142*, 3970-3979.

[9] Guo, F.-S.; Day, B.-M.; Chen, Y.-C.; Tong, M.-L.; Mansikkamäki, A.; Layfield, R. A., *Science*, **2018**, *362*, 1400–1403.

[10] Mannini, M.; Pineider, F.; Sainctavit, P.; Danieli, C.; Otero, E.; Sciancalepore, C.; Talarico, A. M.; Arrio, M.-A.; Cornia, A.; Gatteschi, D.; Sessoli, R., *Nat. Mater.*, **2009**, *8*, 194−197.

[11] Eliseeva, S. V.; Pleshkov, D. N.; Lyssenko, K. A.; Lepnev, L. S.; Bünzli, J.-C. G.; Kuzmina, N. P., *Inorg. Chem.*, **2010**, *49*, 9300−9311.

[12] Miyata, K.; Konno, Y.; Nakanishi, T.; Kobayashi, A.; Kato, M.; Fushimi, K.; Hasegawa, Y., *Angew. Chem., Int. Ed.*, **2013**, *52*, 6413−6416.

[13] Xu, H.; Wang, J.; Wei, Y.; Xie, G.; Xue, Q.; Deng, Z.; Huang, W., *J. Mater. Chem. C*, **2015**, *3*, 1893−1903.

[14] Eliseeva, S. V.; Bünzli, J.-C. G., *Chem. Soc. Rev.*, **2010**, *39*, 189–227.

[15] Hamon, N.; Roux, A.; Beyler, M.; Mulatier, J.-C.; Andraud, C.; Nguyen, C.; Maynadier, M.; Bettache, N.; Duperray, A.; Grichine, A.; Brasselet, S.; Gary-Bobo, M.; Maury, O.; Tripier, R., *J. Am. Chem. Soc.*, **2020**, *142*, 10184–10197.

[16] El Rez, B.; Liu, J.; Béreau, V.; Duhayon, C.; Horino, Y.; Suzuki, T.; Coolen, L.; Sutter, J.-P., *Inorg. Chem. Front.,* **2020**, *7*, 4527–4534.

[17] Huizi-Rayo, U.; Zabala-Lekuona, A.; Terenzi, A.; Cruz, C. M.; Cuerva, J. M.; Rodríguez-Diéguez, A.; Garcia, J. A.; Seco, J. M.; San Sebastián, E.; Cepeda, J., *J. Mater.Chem. C.,* **2020**, *8*, 8243–8256.

[18] Gendron, F.; Di Pietro, S.; Abad Galán, L.; Riobé, F.; Placide, V.; Guy, L.; Zinna, F.; Di Bari, L.; Bensalah-Ledoux, A.; Guyot, Y.; Pilet, G.; Pointillart, F.; Baguenard, B.; Guy, S.; Cador, O.; Maury, O.; Le Guennic, B., *Inorg. Chem. Front.,* **2021**, *8*, 914-926.

[19] Lefeuvre, B.; Mattei, C. A.; Flores González, J.; Gendron, F.; Dorcet, V.; Riobé, F.; Lalli, C.; Le Guennic, B.; Cador, O.; Maury, O.; Guy, S.; Bensalah-Ledoux, A.; Baguenard, B.; Pointillart, F., *Chem. Eur. J.,* **2021**, *27*, 7362-7366.

[20] Long, J.; Rouquette, J.; Thibaud, J.-M.; Ferreira, R. A. S.; Carlos, L. D.; Donnadieu, B.; Vieru, V.; Chibotaru, L. F.; Konczewicz, L; Haines, J.; Guari, Y.; Larionova, J., *Angew. Chem. Int. Ed.*, **2015**, *54*, 2236-2240.

[21] Long, J.; Ivanov, M. S.; Khomchenko, V. A.; Mamontova, E.; Thibaud, J.-M.; Rouquette, J.; Beaudhuin, M.; Granier, D.; Ferreira, R. A. S.; Carlos, L. D.; Donnadieu, B.; Henriques, M. S. C.; António Paixão, J.; Guari, Y.; Larionova, J., *Science*, **2020**, *367*, 671-676.

[22] Wang, K.; Zeng, S.; Wang, H.; Dou, J.; Jiang, J., *Inorg. Chem. Front.*, **2014**, *1*, 167-171.

[23] Atzori, M.; Dhbaibi, K.; Douib, H.; Grasser, M.; Dorcet, V.; Breslavetz, I.; Paillot, K.; Cador, O.; Rikken, G. L. J. A. ; Le Guennic, B.; Crassous, J.; Pointillart, F.; Train, C., *J. Am. Chem. Soc.,* **2021**, *143*, 2671-2675.

[24] Liu, C. M.; Zhang, D.-Q.; Zhu, D.-B., *Inorg. Chem.*, **2013**, *52*, 8933-8940.

[25] Li, D.-P.; Wang, T.-W.; Li, C.-H.; Liu, D.-S.; Li, Y.-Z.; You, X.-Z., *Chem. Commun.,* **2010**, *46*, 2929-2931.

[26] Ou-Yang, J. K.; Saleh, N.; Fernández García, G.; Norel, L.; Pointillart, F. ; Guizouarn, T.; Cador, O.; Totti, F.; Ouahab, L.; Crassous, J.; Le Guennic, B. *Chem. Commun.,* **2016**, *52*, 14474-14477.

[27] Feng, M.; Lyu, B.-H.; Wang, M.-H.; Wu, W.-W.; Chen, Y.-C.; Huang, G.-Z.; Lin, W.-Q.; Wu, S.-G.; Liu, J.-L.; Tong, M.-L. *Inorg. Chem.,* **2019**, *58*, 10694-10703.

[28] Harada, T.; Nakano, Y.; Fujiki, M.; Naito, M.; Kawai, T.; Hasegawa, Y., *Inorg. Chem.,* **2009**, *48*, 11242-11250.

[29] Koiso, N.; Kitagawa, Y.; Nakanishi, T.; Fushimi, K.; Hasegawa, Y., *Inorg. Chem.*, **2017**, *56*, 5741-5747.

[30] Cotter, D.; Dodder, S.; Klimkowski, V. J.; Hopkins, T. A., *Chirality*, **2019**, *31*, 301-311.

[31] Mattei, C. A.; Montigaud, V.; Gendron, F.; Denis-Quanquin, S.; Dorcet, V.; Giraud, N.; Riobé, F.; Argouarch, G.; Maury, O.; Le Guennic, B.; Cador, O.; Lalli, C.; Pointillart, F., *Inorg. Chem. Front.,* **2021**, *8*, 947-962.

[32] Mattei, C. A.; Montigaud, V.; Dorcet, V.; Riobé, F.; Argouarch, G.; Maury, O.; Le Guennic, B.; Cador, O.; Lalli, C.; Pointillart, F., *Inorg. Chem. Front.,* **2021**, *8*, 963-976.

[33] Platt, A. W. G., *Coord. Chem. Rev.,* **2017**, *340*, 62–78.

[34] Furan, S.; Vogt, M.; Winkels, K.; Lork, E.; Mebs, S.; Hupf, E.; Beckmann, J., *Organometallics* **2021**, *40*, 1284-1295.

[35] Llunell, M.; Casanova, D.; Cirera, J.; Alemany, P.; Alvarez, S. SHAPE Program for the Stereochemical Analysis of Molecular Fragments by Means of Continuous Shape Measures and Associated Tools, Departament de Química Física, Departament de Química Inorgànica and Institut de Química Teòrica i Computacional – Universitat de Barcelona, Barcelona, Spain.

[36] Mattei, C. A.; Dhbaibi, K.; Lefeuvre, B.; Dorcet, V.; Argouarch, G.; Cador, O.; Le Guennic, B.; Maury, O.; Lalli, C.; Guy, S.; Bensalah-Ledoux, A.; Riobé, F.; Baguenard, B.; Pointillart, F., *Chirality*, **2022**, *34*, 34-47

[37] Binnemans, K., *Coord. Chem. Rev.*, **2015**, *295*, 1-45.

[38] Harada, T.; Hasegawa, Y.; Nakano, Y.; Fujiki, M.; Naito, M.; Wada, T.; Inoue, Y.; Kawai, T., *J. Alloy. Compd.,* **2009**, *488*, 599–602.

[39] Kishi, Y.; Cornet, L.; Pointillart, F.; Riobé, F.; Lefeuvre, B.; Cador, O.; Le Guennic, B.; Maury, O.; Fujiwara, H.; Ouahab, L., *Eur. J. Inorg. Chem.,* **2018**, *3–4*, 458–468.

[40] Guégan, F.; Jung, J.; Le Guennic, B.; Riobé, F.; Maury, O.; Gillon, B.; Jacquot, J.-F.; Guyot, Y.; Morell, C.; Luneau, D., *Inorg. Chem. Front.,* **2019**, *6*, 3152–3157.

[41] Kahn, O. *Molecular Magnetism*, VCH, Weinhem, **1993**.

[42] Pointillart, F.; Bernot, K.; Golhen, S.; Le Guennic, B.; Guizouarn, T.; Ouahab, L.; Cador, O., *Angew. Chem. Int. Ed.,* **2015**, *54*, 1504-1507.

[43] Tang, J.; Zhang, P. *Lanthanide Single-Ion Molecular Magnets. In Lanthanide Single Molecule Magnets*; Springer-Verlag Berlin Heidelberg, **2015**.

[44] Rousset, E.; Piccardo, M.; Boulon, M.-E.; Gable, R. W.; Soncini, A.; Sorace, L.; Boskovic, C., *Chem. Eur. J.,* **2018**, *24*, 14768–14785.

[45] Handzlik, G.; Magott, M.; Arczyński, M.; Sheveleva, A. M.; Tuna, F.; Baran, S.; Pinkowicz, D., *Dalton Trans.,* **2020**, *49*, 11942–11949.

[46] Ortu, F.; Reta, D.; Ding, Y. S.; Goodwin, C. A. P.; Gregson, M. P.; McInnes, E. J. L.; Winpenny, R. E. P; Zheng, Y. Z.; Liddle, S. T.; Mills, D. P.; Chilton, N. F., *Dalton Trans.*, **2019**, *48*, 8541-5845.

[47] Ullah, A.; Baldovi, J. J.; Gaita-Ariño, A.; Coronado, E., *Dalton. Trans.,* **2021**, *50*, 11071-11076.

[48] Richardson, M. F.; Wagner, W. F.; Sands, D. E., *J. Inorg. Nucl. Chem.*, **1968**, *30*, 1275–1289.

[49] Beckmann, J.; Giang Do, T.; Grabowsky, S.; Hupf, E.; Lork, E.; Mebs, S. *Z. Anorg. Allg. Chem.* **2013**, 2233–2249

[50] Sheldrick, G. M. SHELXT – Integrated space-group and crystal-structure determination, *Acta Crystallogr., Sect. A: Found. Adv.* **2015**, *71*, 3–8.

[51] Sheldrick, G. M. Crystal structure refinement with SHELXL, *Acta Crystallogr., Sect. C: Struct. Chem.* **2015**, *71*, 3–8.

Received: 25 March 2022
Accepted: 24 May 2022

ORCID for authors
Fabrice Pointillart: 0000-0001-7601-1927
Pierre-Antoine Bouit: 0000-0002-0538-9276
François Riobé: 0000-0001-6746-8132
Carlo Andrea Mattei: 0000-0001-5550-9195
Thomas Delouche: 0000-0002-5035-3010
Bertrand Lefeuvre: 0000-0002-9328-4625
Marie Dallon-Cordier: 0000-0003-0917-2725
Claudia Lalli: 0000-0002-1634-716X
Olivier Cador: 0000-0003-2064-6223
Laura Abad Galán: 0000-0001-6226-0850
Olivier Maury: 0000-0002-4639-643X